ELSEVIER

Comput. Methods Appl. Mech. Engrg. 190 (2001) 5009–5026

Computer methods in applied mechanics and engineering

www.elsevier.com/locate/cma

Weakly compressible high-order I-stable central difference schemes for incompressible viscous flows ☆

Weizhu Bao *, Shi Jin [1]

School of Mathematics, Georgia Institute of Technology, Atlanta, Georgia, GA 30332, USA

Received 11 March 2000; received in revised form 12 June 2000

Abstract

In this paper, we propose a weakly compressible model for numerical simulation of the incompressible viscous flows. This model asymptotically approximates the incompressible Navier–Stokes equations when the mach number tends to zero. The main advantage of this model is that its numerical discretization avoids any Poisson solver, thus is very attractive for problems with complicated geometries. This model is discretized by high-order center differences in space and the so-called 'I-stable' method for time. The linear stability region of an I-stable method contains part of the imaginary axis. When solving a system of convection–diffusion equations with a small viscosity, the I-stable method allows a very large cell Reynolds number, thus is particularly suitable for the simulation of fluid flows with large Reynolds numbers. Numerical experiments illustrate the efficiency and robustness of this approach.

1. Introduction

The goal of the paper is to solve numerically the incompressible Navier–Stokes equations

$$\mathbf{u}_t + \nabla \cdot (\mathbf{u}\mathbf{u}) + \nabla p = \frac{1}{Re}\Delta \mathbf{u}, \tag{1.1}$$

$$\nabla \cdot \mathbf{u} = 0 \tag{1.2}$$

on a bounded domain Ω, where $\mathbf{u} = (u_1, u_2)$ is the velocity, p the pressure, Re the Reynolds number and $\mathbf{u}\mathbf{u}$ is the tensor product

$$\mathbf{u}\mathbf{u} = \begin{pmatrix} u_1^2 & u_1 u_2 \\ u_1 u_2 & u_2^2 \end{pmatrix}.$$

One of the main difficulties in solving these equations is the divergence free constraint for $\mathbf{u}$. In order to avoid this condition we propose the following weakly compressible model:

☆ Research supported in part by NSF grant No. DMS-9704957.

* Corresponding author. On leave from Department of Applied Mathematics, Tsinghua University, Beijing 100084, People's Republic of China.

E-mail addresses: wbao@math.gatech.edu (W. Bao), jin@math.gatech.edu, jin@math.wisc.edu (S. Jin).

[1] Present address: Department of Mathematics, University of Wisconsin-Madison, Madison, WI 53706, USA.

0045-7825/01/$ - see front matter
PII: S0045-7825(00)00363-7

$$p_t + \nabla \cdot (p\mathbf{u}) = 0, \tag{1.3}$$

$$\mathbf{u}_t + \nabla \cdot (\mathbf{u}\mathbf{u}) + \frac{1}{M^2}\nabla p = \frac{1}{Re}\Delta \mathbf{u}, \tag{1.4}$$

where M plays the role of the Mach number. Eqs. (1.3) and (1.4) are subject to appropriate initial conditions and boundary conditions. As they are used to approximate incompressible viscous flows, we always assume the boundary conditions satisfy

$$\int_{\partial\Omega} \mathbf{u} \cdot \mathbf{n}\,\mathrm{d}s = 0, \tag{1.5}$$

where Ω denotes the bounded physical domain considered, $\partial\Omega$ denotes the boundary of Ω and $\mathbf{n}$ denotes the unit outward normal vector. In fact (1.5) is a result of the divergence free condition $\nabla \cdot \mathbf{u} = 0$ of an incompressible flow, i.e.,

$$0 = \int_{\Omega} \nabla \cdot \mathbf{u}\,\mathrm{d}\mathbf{x} = \int_{\partial\Omega} \mathbf{u} \cdot \mathbf{n}\,\mathrm{d}s.$$

It is easy to see that, when $M \ll 1$, the weakly compressible model (1.3) and (1.4) asymptotically approaches the incompressible Eqs. (1.1) and (1.2) with an error of $O(M^2)$. Thus, for suitable small Mach number, one can expect that the solution of the weakly compressible model approximates that of the incompressible Navier–Stokes equations.

This approach is motivated by the mathematical study of the zero Mach number limit of the compressible flows, see [17,18,22,23,28]. See also the asymptotic analysis presented in [19,20]. These mathematical theories justify the fact that the incompressible flow Eqs. (1.1) and (1.2) can be used for certain real fluids that are slightly compressible, and vice versa. In practice, there have been vast volumes of literatures where compressible fluid equations were used to solve incompressible or almost incompressible flows, see for examples [11,13,15].

If the goal is just to solve the incompressible flows rather than the compressible flows, then it is not necessary to use the physical compressible Navier–Stokes equations. Rather, one may design simple artificial compressible models that approach to the incompressible equations in the limit of vanishing Mach number. One such approach is the lattice Boltzmann method [3,16], where simple discrete-velocity kinetic models were designed so as to recover the incompressible Navier–Stokes equations for zero Mach number and small mean free path. The advantage of using these weakly compressible models is that it avoids the usage of the Poisson solver, thus provides easy and efficient methods for problems involving complicated geometries. However, one pays two prices for this. First, for small Mach number the convection operator becomes numerically stiff [1,13], thus an explicit method requires a smaller time step than a method that solves directly the incompressible equations. However, in practice one usually takes $0.1 \leqslant M \leqslant 0.3$, so the time step is at most 10 times smaller and it may not be of concern compared with a Poisson solver for complicated geometries. The second is that it is not clear theoretically how small the Mach number should be for a given (possibly very high) Reynolds number such that the error introduced by the weak compressibility does not destroy the desired physical properties of the incompressible flows. For steady-state calculation, this is not an issue since the weakly compressible model becomes the steady-state Navier–Stokes equations exactly. For unsteady problems, our numerical experiments indicate that the effect of weak compressibility is minimum. More theoretical investigation of the point is certainly desirable.

If an efficient Poisson solver is available for the problem to be solved, the projection method, originally introduced by Chorin [6] and Teman [26] and its latest development [9] offers attractive numerical recipes for the incompressible Navier–Stokes equations. Several classes of pseudo-compressible methods, whose origin could be traced back to the work of Chorin [4,5] for steady problem, were also available in the literature, see [25] and references therein. They were put into the framework of a penalty method and need to solve either a nonlinear system or a Poisson or Helmoholtz equation, thus are different from the discretizations proposed here, but the models used for discretization are very closed related to ours.

Unlike the penalty methods, we discretize the Eqs. (1.3) and (1.4) by the fourth-order difference method. High-order centered difference schemes are attractive because they do not introduce any numerical viscosity

that may mix with the physical viscosity. Using a proper cell Reynolds number, the viscous effect observed numerically is purely physical. For time-discretization, it is crucial to use the so-called I-stable method, which has a linear stability region containing part of the imaginary axis, allowing a numerical stability for arbitrary cell Reynolds numbers.

A time-discretization for an ordinary differential equation is called I-stable if the linear stability region contains part of the imaginary axis [2]. In [29,30] Vichnevetsky studied the stability charts in the numerical approximation of partial differential equations. He found that the linear stability regions of some time-discretization schemes contain part of imaginary axis, and then applied these schemes to linear hyperbolic and advection–diffusion equations, which offer remarkable numerical stability for convection–diffusion equations with small or zero diffusion. In fact, this approach removes the constraint on the cell Reynolds number. In [7,8], E and Liu utilized this kind of time discretizations to solve the incompressible Navier–Stokes, and were able to compute incompressible flows with very high Reynolds numbers.

For compressible flows, due to the presence of shocks, one cannot push the cell Reynolds number arbitrarily high if one attempts to resolve the physical shock layer [2]. However, the traditional stability condition, which requires the cell Reynolds number to be less than two, can be lifted to about six when fourth-order center differences are used for space, coupled with the fourth-order Runge–Kutta method (which is I-stable) for time [2].

Based on the positive experience of the high-order I-stable center differences for both compressible and incompressible flows [2,7], we use it for the weakly compressible Eqs. (1.3) and (1.4). It allows the cell Reynolds number Rc to be arbitrarily large, thus is very suitable for large Reynolds number flow simulation.

This paper is organized as follows. In the next section, we obtain the usual incompressible viscous flow equations from (1.3) and (1.4) by performing a formal asymptotic analysis. In Section 3, we introduce the fourth-order I-stable central difference schemes. In Section 4, we present several numerical experiments on both steady and unsteady problems, include the incompressible viscous flows in a driven rectangular cavity, in a channel with a backward-facing step and in a driven triangular cavity. We conclude in Section 5 with some discussions.

2. The incompressible limit of the weakly compressible model

In this section, we obtain the incompressible Navier–Stokes equations by a formal asymptotic analysis on (1.3) and (1.4) assuming a small Mach number M.

2.1. The small Mach number asymptotics

Assume $M \ll 1$, we introduce the following ansatz:

$$\mathbf{u} = \mathbf{u}^{(0)} + M^2\mathbf{u}^{(1)} + \cdots, \tag{2.1}$$

$$p = p^{(0)} + M^2 p^{(1)} + \cdots, \tag{2.2}$$

subject to the boundary conditions:

$$\int_{\partial\Omega} \mathbf{u}^{(i)} \cdot \mathbf{n}\,\mathrm{d}s = 0, \quad i = 0, 1, 2, \ldots \tag{2.3}$$

Inserting (2.1) and (2.2) into the Eqs. (1.3) and (1.4) and matching the coefficients of M^i order by order, then a set of basic and perturbation equations can be obtained. Here we do not list the complete set of these equations, but only those which will give insight of the limit behavior. These are the leading order equations of (1.3)

$$p_t^{(0)} + \nabla \cdot \left(p^{(0)}\mathbf{u}^{(0)}\right) = 0 \tag{2.4}$$

and the leading and first-order equations of (1.4)

$$\nabla p^{(0)} = 0, \tag{2.5}$$

$$\mathbf{u}_t^{(0)} + \nabla \cdot \left(\mathbf{u}^{(0)}\mathbf{u}^{(0)}\right) + \nabla p^{(1)} = \frac{1}{Re}\Delta \mathbf{u}^{(0)}. \tag{2.6}$$

From Eq. (2.5), one knows that $p^{(0)}$ does not depend on $\mathbf{x}$. Thus it can be assumed that

$$p^{(0)} = p^{(0)}(t). \tag{2.7}$$

Substituting (2.7) into (2.4) gives

$$p_t^{(0)}(t) + p^{(0)}(t)\nabla \cdot \mathbf{u}^{(0)} = 0. \tag{2.8}$$

Integrating on the physical domain Ω and using (2.3), one gets

$$p_t^{(0)}(t) = -\frac{p^{(0)}(t)}{|\Omega|}\int_\Omega \nabla \cdot \mathbf{u}^{(0)}\,\mathrm{d}\mathbf{x} = -\frac{p^{(0)}(t)}{|\Omega|}\int_{\partial\Omega} \mathbf{u}^{(0)} \cdot \mathbf{n}\,\mathrm{d}s = 0, \tag{2.9}$$

where $|\Omega|$ is the area of the domain Ω. This implies that $p^{(0)}$ does not depend on t either, i.e., $p^{(0)}$ is a constant. Assuming

$$p^{(0)} \equiv p_0 = \text{constant}. \tag{2.10}$$

Inserting (2.10) back into the Eq. (2.4) gives

$$\nabla \cdot \mathbf{u}^{(0)} = 0. \tag{2.11}$$

Thus the leading order of $\mathbf{u}$ satisfies the incompressibility condition. Now (2.11), coupled with (2.6), are the incompressible Navier–Stokes equations

$$\mathbf{u}_t^{(0)} + \nabla \cdot (\mathbf{u}^{(0)}\mathbf{u}^{(0)}) + \nabla p^{(1)} = \frac{1}{Re}\Delta \mathbf{u}^{(0)}, \tag{2.12}$$

$$\nabla \cdot \mathbf{u}^{(0)} = 0. \tag{2.13}$$

From this asymptotic analysis, one can see that $p^{(1)}$ plays the role of the pressure in the incompressible viscous flow Eqs. (1.1) and (1.2). In fact, $p^{(1)}$ can be obtained in the following way:

$$\frac{1}{M^2}(p - \bar{p}) \to p^{(1)} \quad \text{when } M \to 0, \tag{2.14}$$

where $\bar{p} = 1/|\Omega| \int_\Omega p\,\mathrm{d}\mathbf{x}$ is the mean value of p in the domain Ω.

The above asymptotic analysis shows that the weakly compressible model (1.3) and (1.4) approximates the incompressible Navier–Stokes equations (1.1) and (1.2) with a second-order error in M.

2.2. Connection with the compressible Navier–Stokes equations

Consider the dimensionless compressible Navier–Stokes equations in the conservation form [20,21]

$$\rho_t + \nabla \cdot (\rho\mathbf{u}) = 0, \tag{2.15}$$

$$(\rho\mathbf{u})_t + \nabla \cdot ((\rho\mathbf{u})\mathbf{u}) + \frac{1}{M^2}\nabla p = \nabla \cdot \tau, \tag{2.16}$$

$$e_t + \nabla \cdot (\mathbf{u}(e + p)) = \nabla \cdot (\tau\mathbf{u}) + \nabla \cdot \mathbf{q}, \tag{2.17}$$

where ρ is the density, $\mathbf{u}$ the velocity, p the pressure, e the total energy per unit volume, τ the viscous stress tensor, $\mathbf{q}$ the heat flux and M is the Mach number. To show its connection with the weakly compressible model (1.3) and (1.4), we use the equation of state of a perfect gas, assume that the heat flux q is zero, namely

$$p = \rho\varepsilon, \quad e = \rho\varepsilon + \frac{M^2}{2}\rho\mathbf{u}^2, \tag{2.18}$$

where ε is the specific internal energy. Substituting (2.18) into (2.17) and after some manipulations, one obtains

$$\rho_t + \nabla\cdot(\rho\mathbf{u}) = 0, \tag{2.19}$$

$$\mathbf{u}_t + \nabla\cdot(\mathbf{u}\mathbf{u}) + \frac{1}{\rho M^2}\nabla p = \frac{1}{\rho Re}\Delta\mathbf{u} + \frac{1}{3\rho Re}\nabla(\nabla\cdot\mathbf{u}) + \mathbf{u}\nabla\cdot\mathbf{u}, \tag{2.20}$$

$$p_t + \nabla\cdot(p\mathbf{u}) = -p\nabla\cdot\mathbf{u}. \tag{2.21}$$

When the Mach number M is small, the density ρ almost does not change [21] and the divergence free condition on the velocity $\mathbf{u}$, i.e. $\nabla\cdot\mathbf{u} = 0$ is almost satisfied by a formal asymptotic analysis [22]. Thus Eqs. (1.3) and (1.4) can be obtained from (2.19)–(2.21) by choosing $\rho = 1$ and zeroing $\nabla\cdot\mathbf{u}$. We can see that the role of p in (1.3) and (1.4) is the same as that of the p in the compressible viscous flow Eqs. (2.15)–(2.17).

3. Numerical discretization

To solve (1.3) and (1.4), we use the method of line, which decouples the spatial discretization from the temporal discretization. We use high-order central difference schemes for the spatial derivatives in order to achieve high-order accuracy, while in time we use I-stable ODE solvers, which has a remarkable stability for problems with a small viscosity or a high Reynolds number.

3.1. High-order center differences for spatial derivatives

Let $\mathscr{T}_h$ be a rectangular grid of the physical domain Ω and h be the spatial mesh size. Define the following second-order central spatial difference operators:

$$D_x^{(2)}v(x,y) = \frac{1}{2h}[v(x+h,y) - v(x-h,y)], \tag{3.1}$$

$$D_y^{(2)}v(x,y) = \frac{1}{2h}[v(x,y+h) - v(x,y-h)], \tag{3.2}$$

$$\nabla_h^{(2)} = \left(D_x^{(2)}, D_y^{(2)}\right), \tag{3.3}$$

$$\Delta_h^{(2)}v(x,y) = \frac{1}{h^2}[v(x-h,y) + v(x+h,y) + v(x,y-h) + v(x,y+h) - 4v(x,y)]. \tag{3.4}$$

Then the second-order semi-discrete scheme for (1.3) and (1.4) is

$$\frac{\mathrm{d}p}{\mathrm{d}t} + \nabla_h^{(2)}\cdot(p\mathbf{u}) = 0, \tag{3.5}$$

$$\frac{\mathrm{d}\mathbf{u}}{\mathrm{d}t} + \nabla_h^{(2)}\cdot(\mathbf{u}\mathbf{u}) + \frac{1}{M^2}\nabla_h^{(2)}p = \frac{1}{Re}\Delta_h^{(2)}\mathbf{u}. \tag{3.6}$$

We also define the following fourth-order central spatial difference operators:

$$D_x^{(4)}v(x,y) = \frac{1}{12h}[v(x-2h,y) - 8v(x-h,y) + 8v(x+h,y) - v(x+2h,y)], \tag{3.7}$$

$$D_y^{(4)}v(x,y) = \frac{1}{12h}[v(x,y-2h) - 8v(x,y-h) + 8v(x,y+h) - v(x,y+2h)], \tag{3.8}$$

$$\nabla_h^{(4)} = \left(D_x^{(4)}, D_y^{(4)}\right), \tag{3.9}$$

$$\Delta_h^{(4)} v(x,y) = \frac{1}{12h^2}[-v(x-2h,y) - v(x+2h,y) - v(x,y-2h) - v(x,y+2h) + 16v(x-h,y) + 16v(x,y+h) + 16v(x+h,y) + 16v(x,y-h) - 60v(x,y)]. \tag{3.10}$$

Then the fourth-order semi-discrete method is

$$\frac{\mathrm{d}p}{\mathrm{d}t} + \nabla_h^{(4)} \cdot (p\mathbf{u}) = 0, \tag{3.11}$$

$$\frac{\mathrm{d}\mathbf{u}}{\mathrm{d}t} + \nabla_h^{(4)} \cdot (\mathbf{u}\mathbf{u}) + \frac{1}{M^2}\nabla_h^{(4)} p = \frac{1}{Re}\Delta_h^{(4)}\mathbf{u}. \tag{3.12}$$

The discrete systems (3.5) and (3.6) or (3.11) and (3.12) hold at all interior points. The corresponding boundary conditions are discretized by using "ghost points" as in [2]. For example, suppose $\Gamma = \{(x,0) : a \leqslant x \leqslant b\}$ is a boundary and the Dirichlet boundary condition or Neumann boundary condition is posed. We always use the ghost points $(x_j, -h)$.

(1) For the Dirichlet boundary condition $v(x,0) = v_0(x)$, the fourth-order numerical boundary conditions are

$$v(x_j,0) = v_0(x_j), \tag{3.13}$$

$$v(x_j,-h) = 5v(x_j,0) - 10v(x_j,h) + 10v(x_j,2h) - 5v(x_j,3h) + v(x_j,4h). \tag{3.14}$$

(2) For the Neumann boundary condition $(\partial v/\partial y)(x,0) = g(x)$, the fourth-order numerical boundary conditions are

$$v(x_j,0) = \frac{48}{25}v(x_j,h) - \frac{36}{25}v(x_j,2h) + \frac{16}{25}v(x_j,3h) - \frac{3}{25}v(x_j,4h) - \frac{12h}{25}g(x_j), \tag{3.15}$$

$$v(x_j,-h) = \frac{1}{3}\left[-10v(x_j,0) + 18v(x_j,h) - 6v(x_j,2h) + v(x_j,3h)\right] - 4hg(x_j). \tag{3.16}$$

The above Eqs. (3.13)–(3.16) are obtained by Taylor expansions. The boundary conditions at other sides are dealt with in a similar way.

3.2. I-stable time-discretization

A numerical method for the ordinary differential equations

$$\frac{\mathrm{d}\mathbf{U}}{\mathrm{d}t} = \mathbf{F}(\mathbf{U}), \tag{3.17}$$

where $\mathbf{U} = \mathbf{U}(t)$ is a vector function of t and $\mathbf{F}$ is a vector function of $\mathbf{U}$, is called I-stable if its linear stability region includes part of the imaginary axis [2]. Examples of I-stable method include the third- and fourth-Runge–Kutta method, and counter examples include the forward Euler and second-order Runge–Kutta methods [7]. The reason to use I-stable method for problems with small viscosity is that, if a centered difference is used for the convection, a non-I-stable method has a severe Rc constraint. For example, the forward Euler method requires $Rc = hRe \max \mathbf{u} \leqslant 2$. This prevents the simulation of flows with very large Reynolds number unless an extremely fine spatial grid is used. An I-stable method eliminates this kind of constraints and Rc can be infinite [7]. This greatly improves the solvability of flows with a high Reynolds number.

Of course in real applications, if one wants to resolve the effect of physical viscosity, namely, one wants to obtain the solution of the Navier–Stokes equations instead of the Euler equations, Rc should not be taken arbitrarily large. For an incompressible flow, given the Reynolds number Re, the largest possible gird is $O(\sqrt{1/Re})$ [7].

For this reason, we use the classical fourth-order Runge–Kutta method for (3.17).

4. Numerical examples

In this section, we use the schemes in the above section to solve several problems of incompressible viscous flows. In Examples 1–4, we solve several steady problems. In Examples 5 and 6, two unsteady problems are solved. In Examples 1, 2, 5 and 6, we use the fourth-order central spatial difference scheme (3.11) and (3.12). In Examples 3 and 4, the second-order central spatial difference schemes (3.5) and (3.6) are used. The time-discretization for all the examples is the fourth-order Runge–Kutta method. In our computation, we use the Neumann boundary condition for p in (1.3) and (1.4), i.e., $\partial p/\partial \mathbf{n}|_{\partial\Omega} = 0$.

Example 1. The driven cavity flow with the top moving at a uniform velocity.

As shown in Fig. 1(a), the fluid domain is a unit square and the velocity boundary conditions are of zero velocity on the entire boundary except for the upper side of the square where the tangential velocity is equal to 1; the velocity at the corner nodes is fixed to zero to avoid inflow and outflow of the fluid through the first two vertical sides near the corners. A uniform 100×100 mesh is used in our computation. We take $M = 0.1$ and choose $\Delta t = 0.001$. Figs. 2–4 show the steady-state solutions of the velocity field and contour of streamline function for $Re = 100$, 400 and 600, respectively.

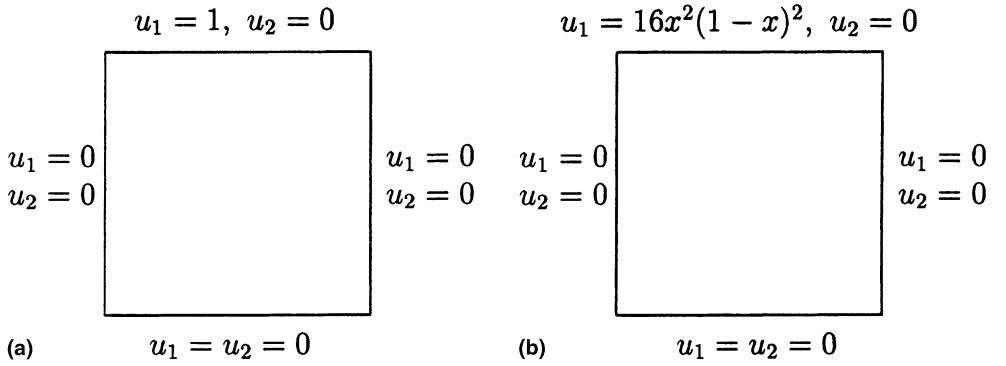

Fig. 1. Setup for: (a) Example 1; (b) Example 2.

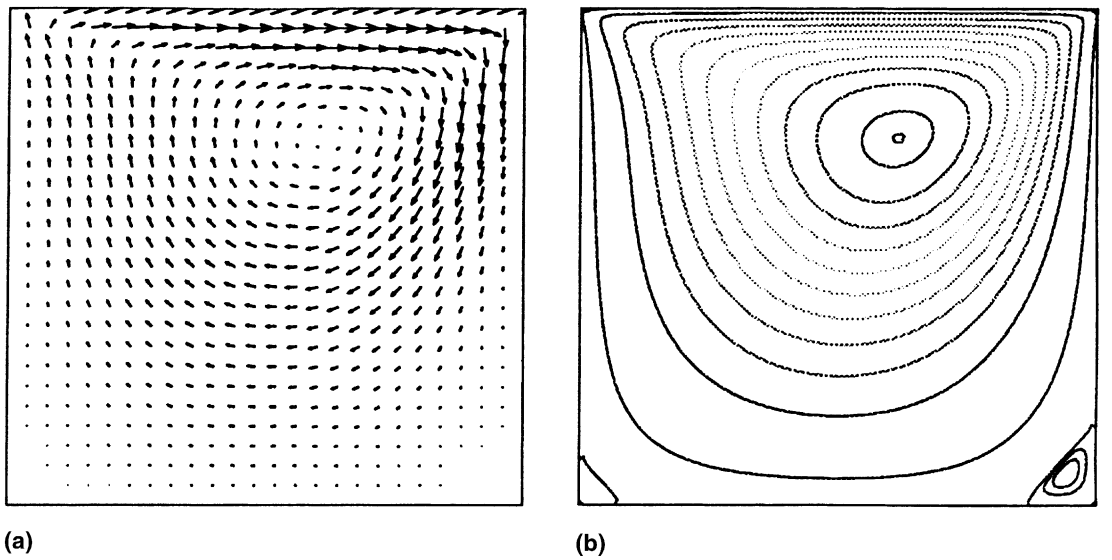

Fig. 2. Numerical solutions of Example 1 with $Re = 100$. (a) Velocity field. (b) Contour of the streamline function.

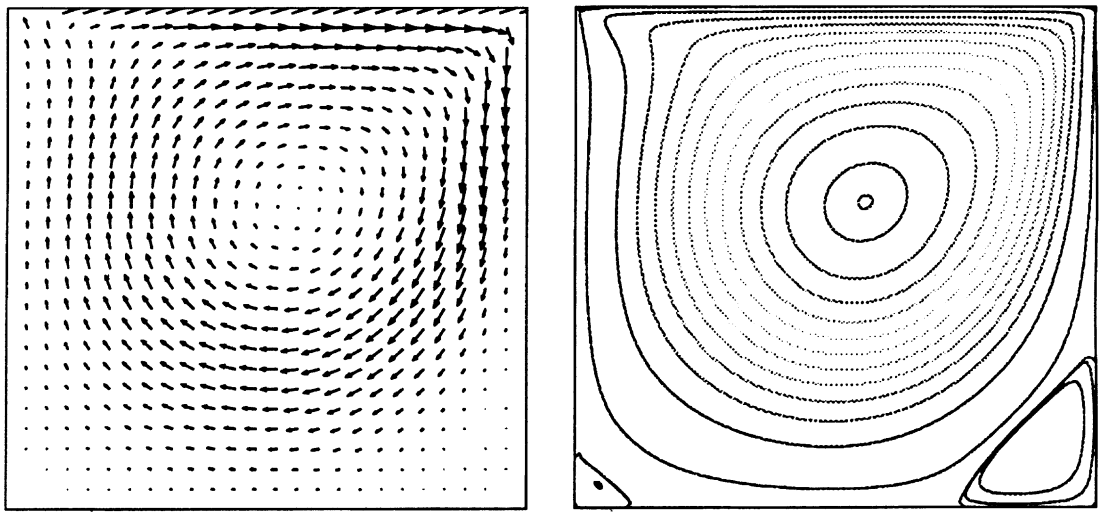

Fig. 3. Numerical solutions of Example 1 with $Re = 400$. (a) Velocity field. (b) Contour of the streamline function.

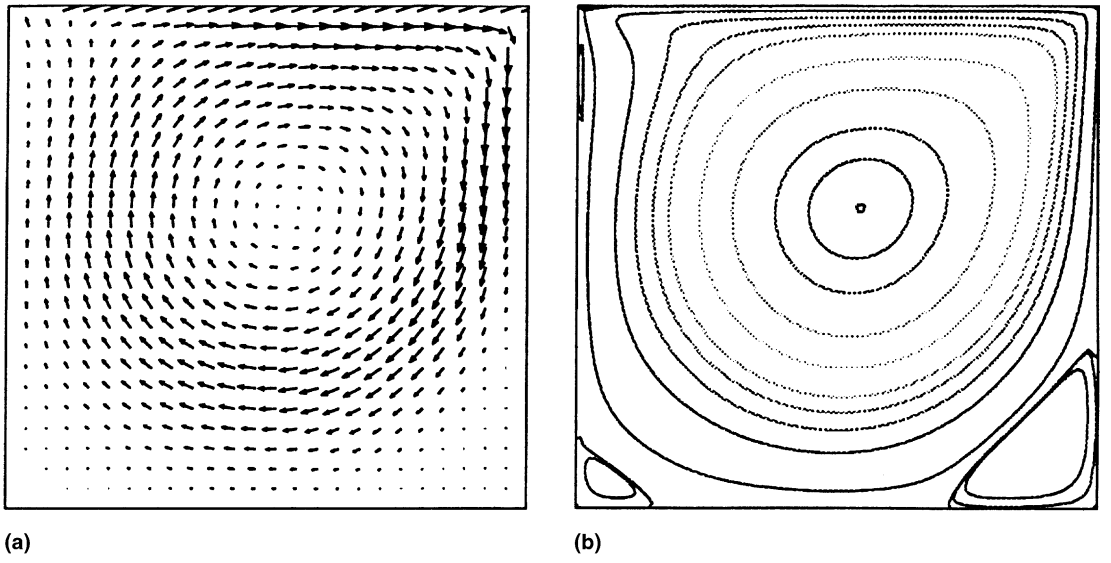

Fig. 4. Numerical solutions of Example 1 with $Re = 600$. (a) Velocity field. (b) Contour of the streamline function.

The results shown in Figs. 2–4 agree very well with the results in Ghia et al. [10] and Hou et al. [16].

Example 2. The driven cavity flow with the top moving with velocity $u_b(x) = 16x^2(1-x)^2$.

As shown in Fig. 1(b), the fluid in the unit square cavity is driven by the moving top at a velocity $u_1 = u_b(x) = 16x^2(1-x)^2$. We take $M = 0.1$ and choose $\Delta t = 0.0005$. Figs. 5–10 show the steady-state solutions of the velocity field and contour of streamline function for $Re = 100$, 400, 1000, 4000, 5000 and 7500 on a uniform mesh 200×200, respectively. We also use this example to test the compressibility effect.

To test the compressibility effect, one quantity that represents compressibility is the mean variation of pressure. The mean pressure is defined as

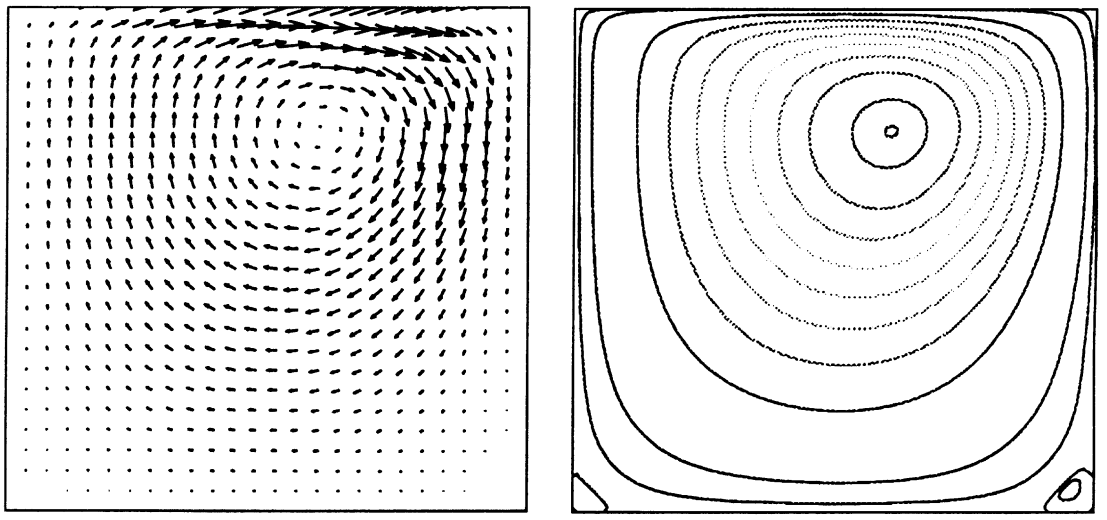

Fig. 5. Numerical solutions of Example 2 with $Re = 100$. (a) Velocity field. (b) Contour of the streamline function.

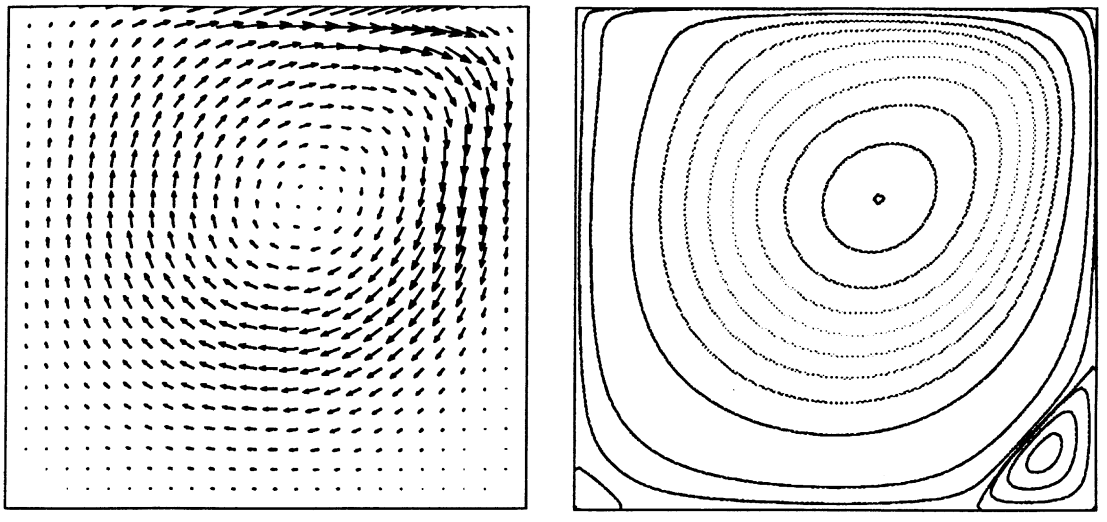

Fig. 6. Numerical solutions of Example 2 with $Re = 400$. (a) Velocity field. (b) Contour of the streamline function.

$$\bar{p} = \frac{\sum_{i,j} p}{N},$$

where N is the total number of grid points. Its mean variation is given by

$$\Delta = \frac{1}{\bar{p}} \sqrt{\sum_{i,j} (p - \bar{p})^2 / N}.$$

For $Re = 100$ on a uniform 100×100 mesh, Δ is calculated for $M = 0.1$, $M = 0.05$, $M = 0.01$ and $M = 0.005$ and listed in Table 1. These results agree with the asymptotic limit (2.14) that Δ is proportional to M^2. These values can be used as a quantitative measure of the compressibility error of the model (1.3) and (1.4). The mean pressure fluctuation with Re is calculated for $M = 0.1$ on a uniform 200×200 mesh

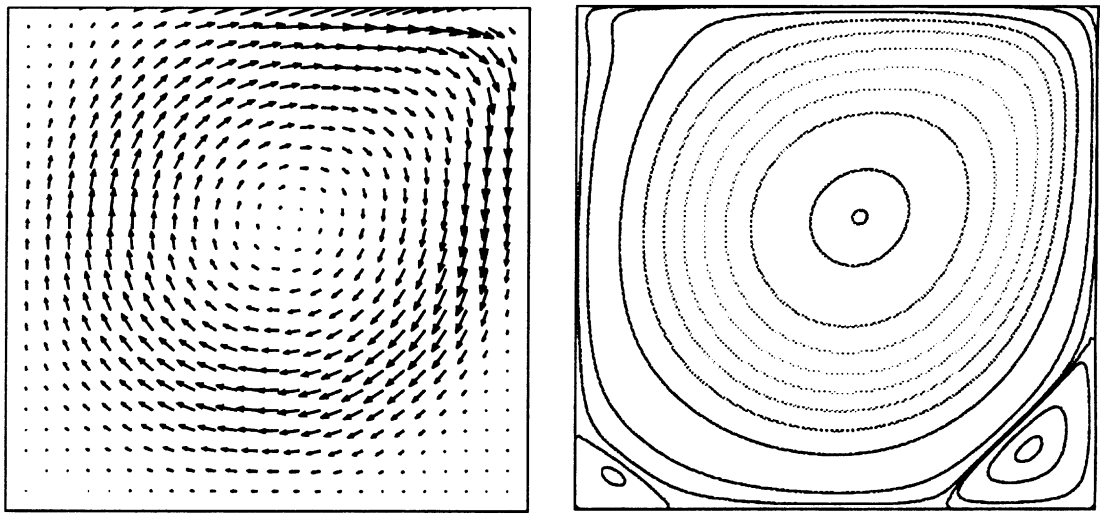

Fig. 7. Numerical solutions of Example 2 with $Re = 1000$. (a) Velocity field. (b) Contour of the streamline function.

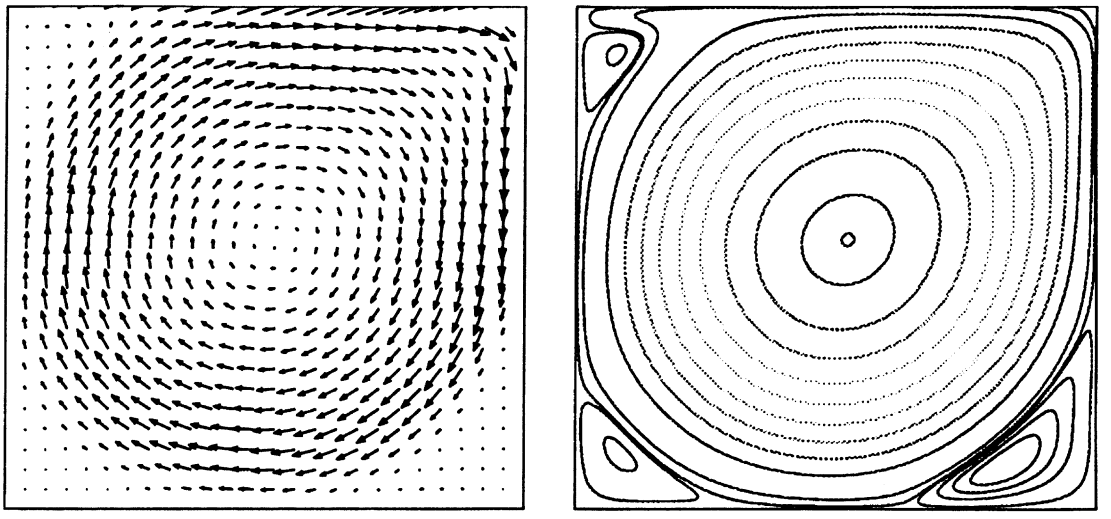

Fig. 8. Numerical solutions of Example 2 with $Re = 4000$. (a) Velocity field. (b) Contour of the streamline function.

and listed in Table 2. The mean pressure fluctuation does not vary very much with Re. With increasing Re, the error decreases slightly, but remains the same order of magnitude. Similar conclusion was obtained in Hou et al. [16] by using the lattice Boltzmann method for the mean variation of density.

The compressibility effect can also be examined for this problem as follows. In the steady case, the Eq. (1.3) is $\nabla \cdot (p\mathbf{u}) = 0$. Due to a non-constant p, the velocity $\mathbf{u}$ does not satisfy the incompressible continuity equation given by $\nabla \cdot \mathbf{u} = 0$ exactly. It is from this equation that the stream function can be defined using $u_1 = \partial\psi/\partial y$ and $u_2 = -\partial\psi/\partial x$, where ψ is the stream function. In fact, there is actually no exact definition for the stream function in the model (1.3) and (1.4). Given a discrete velocity field obtained from the model (1.3) and (1.4), an approximation of the stream function for the incompressible flow with $\nabla \cdot \mathbf{u} = 0$ needs to be constructed. The stream function definition written as $\psi = \int -u_2\,\mathrm{d}x + u_1\,\mathrm{d}y$ is still used to calculate the stream function. When integrating in only the x- or y-direction, the integral becomes $\psi = \int_0^y u_1\,\mathrm{d}y$, or

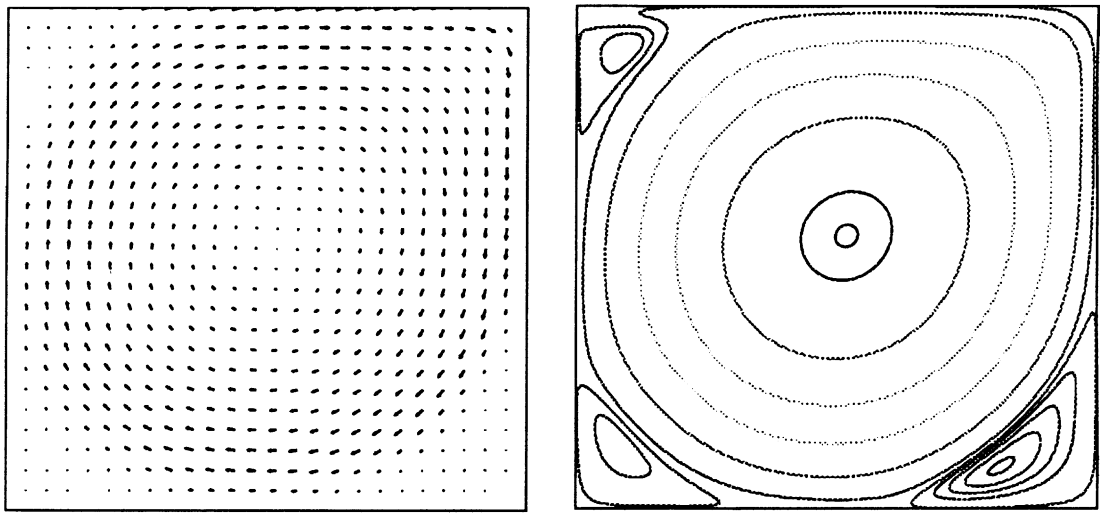

Fig. 9. Numerical solutions of Example 2 with $Re = 5000$. (a) Velocity field. (b) Contour of the streamline function.

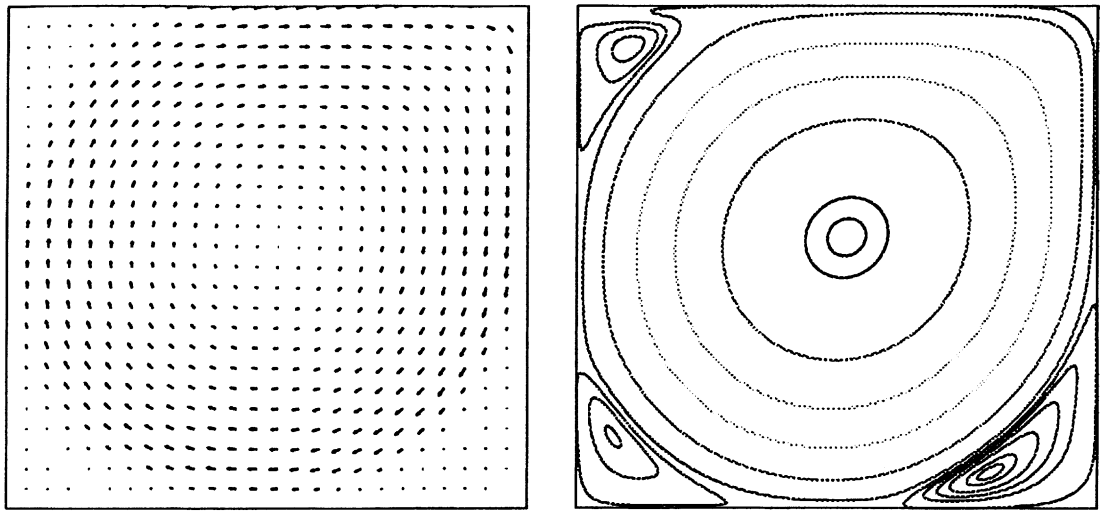

Fig. 10. Numerical solutions of Example 2 with $Re = 7500$. (a) Velocity field. (b) Contour of the streamline function.

Table 1
Mean pressure fluctuation with the Mach number M

M	0.1	0.05	0.01	0.005
Δ	3.63E−4	9.06E−5	3.63E−6	1.04E−6

$\psi = -\int_0^x u_2\,\mathrm{d}x$. In the present example, the boundaries coincide with the zero stream function. The integral then takes the form

$$\psi = \int_0^1 u_1\,\mathrm{d}y = \int_0^1 u_2\,\mathrm{d}x = 0.$$

Table 2
Mean pressure fluctuation with the Reynolds number *Re*

Re	100	400	1000	4000	5000	7500
Δ	3.51E−4	2.61E−4	2.50E−4	2.43E−4	2.41E−4	2.35E−4

In the actual computations, however, the stream function at the end wall will not exactly equal zero because of compressibility, roundoff and integration errors. If the stream function is calculated by integrating u_1 from the bottom to the top edge of the cavity, then the roundoff and integration errors can be omitted comparing to the error lead by compressibility [16]. Thus the mean and maximum value of ψ at the top wall can be computed as an indicator of error due to compressibility. The mean and maximum stream function at the top edge of the cavity is defined, respectively, as

$$S_a = \sqrt{\sum_i (\psi^2(i, n_y))/n_x}$$

and

$$S_m = \max_i |\psi(i, n_y)|,$$

where n_x and n_y are the number of nodes in the x- and y-directions, respectively. These values are calculated for $M = 0.1$ in a uniform 200×200 mesh with different *Re* and listed in Table 3. The compressibility error does not vary very much with *Re*. With increasing *Re*, the error decreases slightly, but it is still of the same order of magnitude. Similar measure and conclusion were used and obtained in Hou et al. [16] by using the lattice Boltzmann method.

From these tests, we can see that the model (1.3) and (1.4) is a good model for numerical simulation of incompressible viscous flows under small Mach number M, at least for steady-state solutions. From our computation experience, usually $M = 0.1$ gives reasonable results. The compressibility effect almost does not depend on the Reynolds number *Re*. Thus when one wants to compute high Reynolds flows, i.e., *Re* becomes larger, it is not necessary to choose a smaller Mach number M.

Example 3. Flow in a backward-facing step channel.

As shown in Fig. 11(a), the fluid is in a backward-facing step channel. The inflow condition is chosen as the Poiseuille profile: $\mathbf{u} = \mathbf{u}_{\text{in}}(y) = (U(y), 0)^{\mathrm{T}}$ for $H/2 \leqslant y \leqslant H$ with $U(y) = 16(H - y)(y - H/2)/H^2$. The outflow boundary condition is chosen as the Neumann boundary condition: $\partial\mathbf{u}/\partial x = 0$. No-slip boundary condition is chosen on the upper and lower solid walls and on the vertical side of the step. We take $M = 0.1$, $H = 0.5$ and $L = 2.5$. A uniform rectangular mesh 500×100 is used in our computation. We choose $\Delta t = 0.0005$. Figs. 12–14 show the steady-state solutions of the velocity field and contour of streamline function for $Re = 100$, 400 and 800, respectively.

These results agree very well with the previous results in Han and Bao [14] and Guermond and Quartapelle [12].

Example 4. The driven triangular cavity.

Table 3
Compressibility effect with the Reynolds number *Re*

Re	100	400	1000	4000	5000
S_a	8.69E−4	3.21E−4	1.25E−4	1.10E−4	9.99E−5
S_m	1.25E−3	5.06E−4	2.20E−4	1.97E−4	1.75E−4

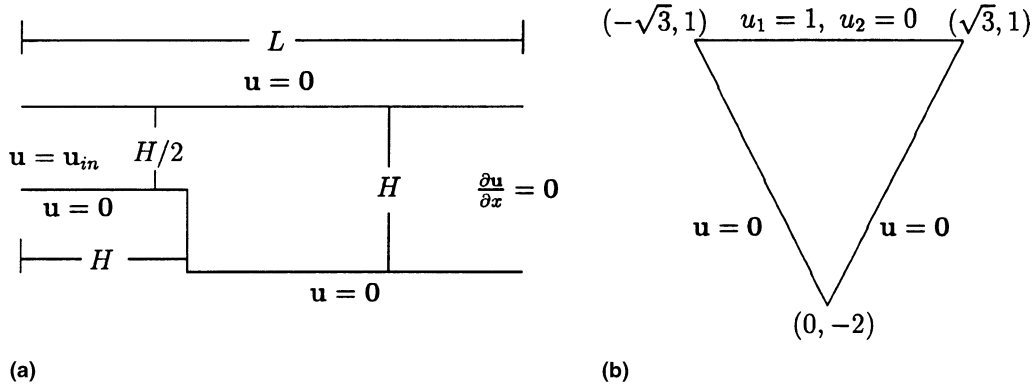

Fig. 11. Setup for: (a) Example 3; (b) Example 4.

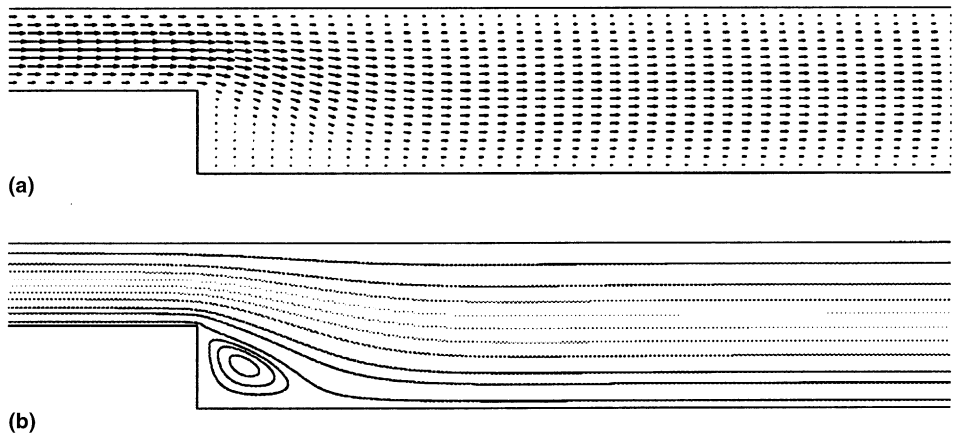

Fig. 12. Numerical solutions of Example 3 with $Re = 100$. (a) Velocity field. (b) Contour of the streamline function.

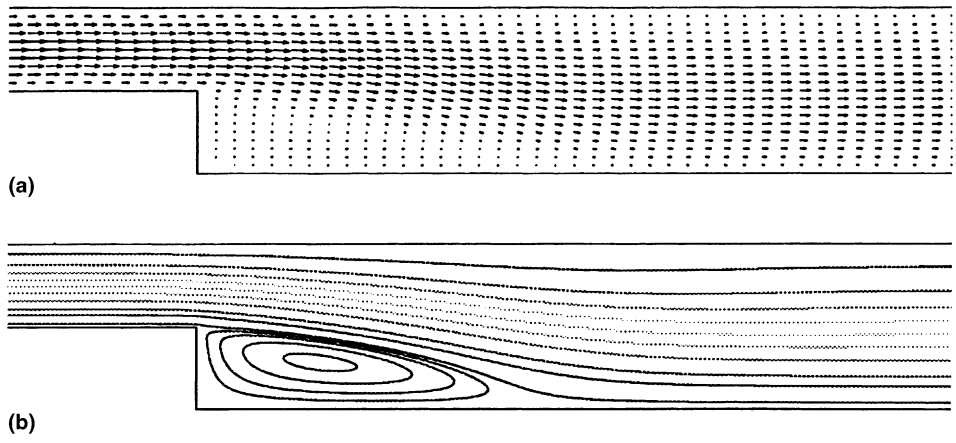

Fig. 13. Numerical solutions of Example 3 with $Re = 400$. (a) Velocity field. (b) Contour of the streamline function.

As shown in Fig. 11(b), the fluid is in a driven triangular cavity. The domain is an equilateral triangle with vertices $(0, -2)$ and $(\pm\sqrt{3}, 1)$. The top horizontal wall is sliding with a uniform velocity 1. A rectangular mesh with 200 vertical lines and 100 horizontal lines is used in our computation. We take $M = 0.1$ and choose $\Delta t = 0.001$. Figs. 15–17 show the steady-state solutions of the velocity field and contour of streamline function for $Re = 100$, 200 and 500, respectively.

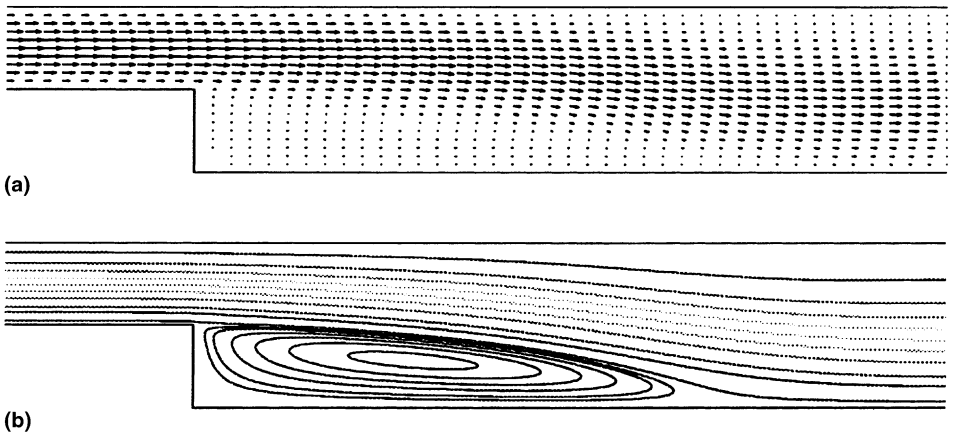

Fig. 14. Numerical solutions of Example 3 with $Re = 800$. (a) Velocity field. (b) Contour of the streamline function.

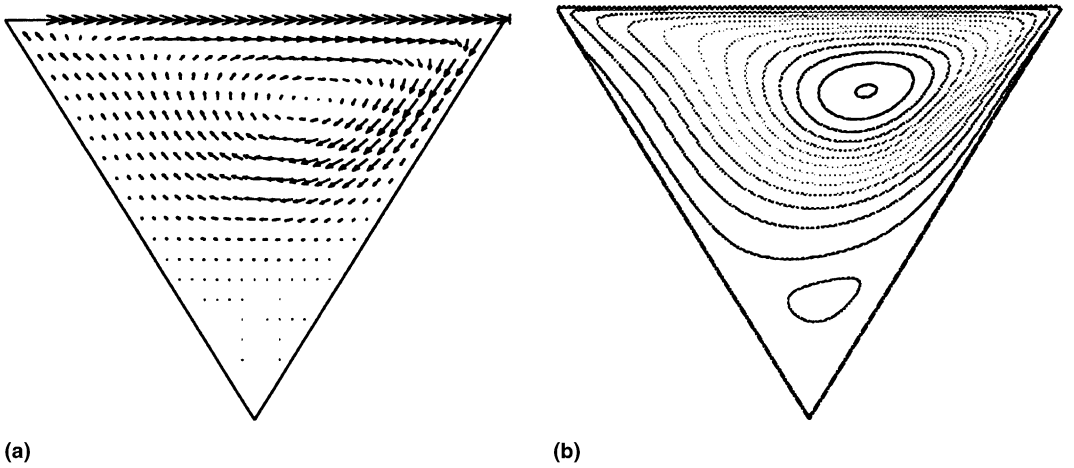

Fig. 15. Numerical solutions of Example 4 with $Re = 100$. (a) Velocity field. (b) Contour of the streamline function.

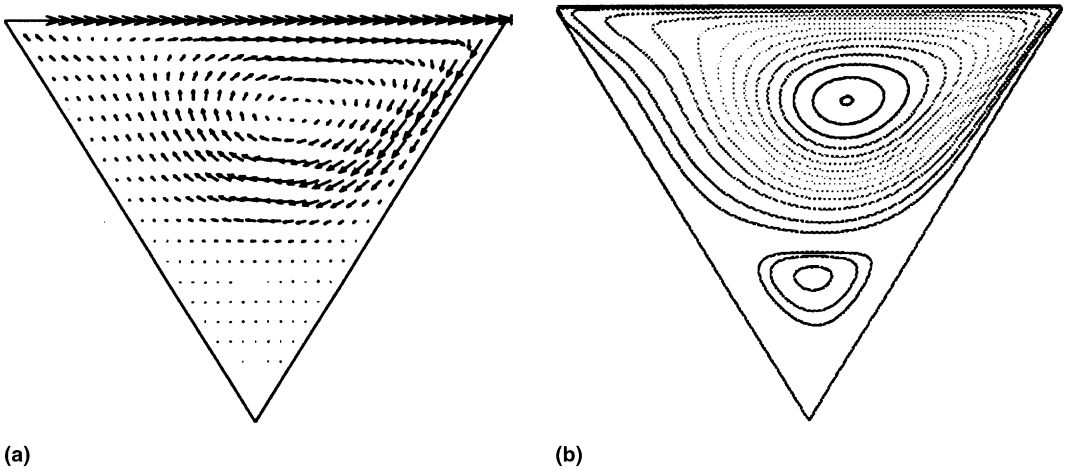

Fig. 16. Numerical solutions of Example 4 with $Re = 200$. (a) Velocity field. (b) Contour of the streamline function.

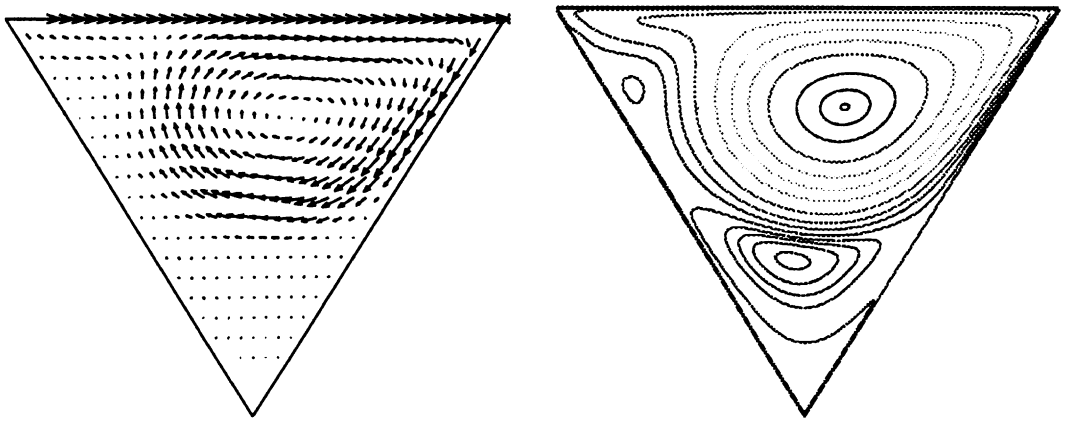

Fig. 17. Numerical solutions of Example 4 with $Re = 500$. (a) Velocity field. (b) Contour of the streamline function.

These results agree very well with the previous results in Ribbens et al. [24] and Guermond and Quartapelle [12].

Example 5. An unsteady driven cavity flow with the top moving at a uniform velocity.

The setup of this example is the same as that in the Example 1 except that we stop at several earlier times before steady state. The initial conditions are

$$p(x,y,0) \equiv 1, \quad \mathbf{u}(x,y,0) = \begin{cases} 1 & \text{for} \quad y = 1, \ 0 < x < 1, \\ 0 & \text{for} \quad 0 \leqslant y < 1, \ 0 \leqslant x \leqslant 1. \end{cases}$$

A uniform 100×100 mesh is used in our computation. We take $M = 0.1$, $Re = 400$ and choose $\Delta t = 0.001$.

The compressibility effect, measured by the mean pressure fluctuation (Δ) and the mean and maximum stream function at the top edge of the cavity (S_a and S_m) as defined in Example 2, are listed in Table 4 at several different times. Fig. 18 shows the solutions of the velocity field and contour of streamline function at times $t = 2.0$, $t = 4.0$, $t = 6.0$ and $t = 8.0$.

These results agree very well with the previous results in Tezduyar et al. [27]. From Table 4 and Fig. 18, one sees that the compressibility effect almost does not depend on time t.

Example 6. An unsteady driven cavity flow with the top moving with velocity $u_b(x) = 16x^2(1-x)^2$.

The setup of this example is the same as that in the Example 2 except that we stop at earlier time before steady state. The initial conditions are

$$p(x,y,0) \equiv 1, \quad \mathbf{u}(x,y,0) = \begin{cases} 16x^2(1-x)^2 & \text{for} \quad y = 1, \ 0 \leqslant x \leqslant 1, \\ 0 & \text{for} \quad 0 \leqslant y < 1, \ 0 \leqslant x \leqslant 1. \end{cases}$$

The choice of $u_b(x)$ and the initial data make the solution smooth in the whole domain. A uniform 200×200 mesh is used in our computation. We take $M = 0.1$ and choose $\Delta t = 0.0005$.

Table 4
Compressibility effect for an unsteady flow at different times

t	2.0	4.0	6.0	8.0	10.0
Δ	6.269E−4	5.310E−4	4.823E−4	4.856E−4	5.087E−4
S_a	2.052E−3	5.754E−4	8.588E−4	7.579E−4	5.643E−4
S_m	4.072E−3	3.967E−3	3.933E−3	3.936E−3	3.954E−3

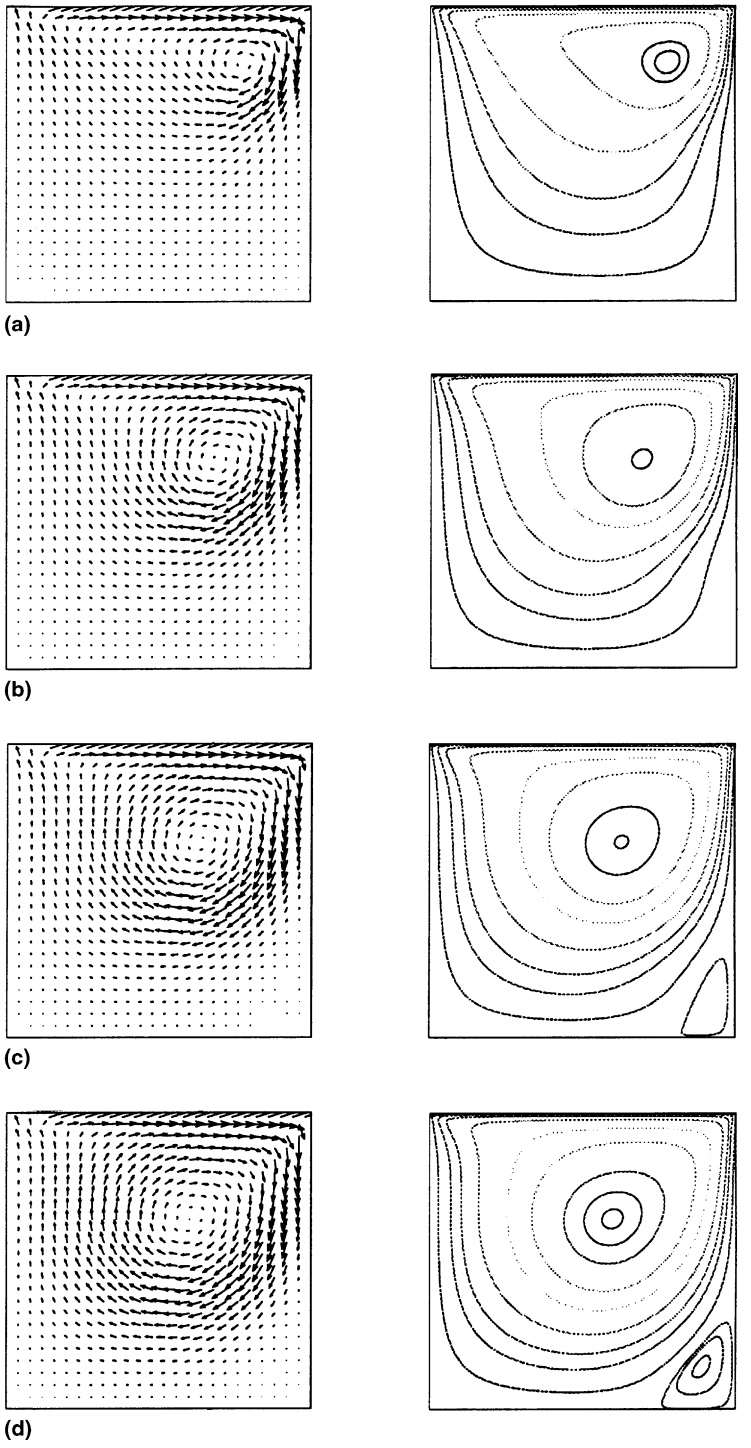

Fig. 18. Numerical solutions of Example 5 at different times. (a) $t = 2.0$, (b) $t = 4.0$, (c) $t = 6.0$, (d) $t = 8.0$. Left: velocity field; right: contour of the streamline function.

The compressibility effect, measured by the mean pressure fluctuation (Δ) and the mean and maximum stream function at the top edge of the cavity (S_a and S_m) at time $t = 1.0$, are listed in Table 5 for different Reynolds number Re.

Table 5
Compressibility effect of an unsteady flow for different Reynolds numbers *Re*

Re	100	400	1000	4000	5000
Δ	5.5259E−4	3.9306E−4	2.7246E−4	1.6401E−4	1.5040E−4
S_a	2.6252E−3	2.5540E−3	1.9803E−3	1.0605E−3	9.0656E−4
S_m	3.7788E−3	3.8141E−3	2.9809E−3	1.6046E−3	1.3909E−3

From Table 5, we can see that the compressibility effect almost does not depend on the Reynolds number *Re* for the unsteady flows. With increasing *Re*, the error decreases slightly, but it remains the same order of magnitude.

From these tests, we can see that the model (1.3) and (1.4) with a small (around 0.1) mach number, is a good model for numerical simulation of steady and unsteady incompressible viscous flows. The compressibility effect almost does not depend on the Reynolds number *Re*, and does not increase in time.

5. Conclusions

In this paper, we propose a weakly compressible model for solving incompressible viscous flow problems. By applying the high-order I-stable central difference schemes, good accuracy and resolution are obtained and large cell Reynolds number can be used. The merit of this method is that one avoids to solve any Poisson equation or Stokes equations. Our numerical results show that, for both steady and unsteady problems, the compressibility error does not vary very much with the Reynolds number *Re* or time. Thus one needs not to choose a smaller M when computing incompressible viscous flows with a larger Reynolds number *Re*. Usually, $M = 0.1$ gives very promising results.

References

[1] S. Abarbanel, P. Duth, D. Gottlieb, Splitting methods for low mach number Euler and Navier–Stokes equations, Comput. Fluids 17 (1989) 1–12.
[2] W. Bao, S. Jin, High-order I-stable central difference schemes for viscous compressible flows, J. Comput. Math., submitted.
[3] S. Chen, G. Doolen, Lattice Boltzmann method for fluid flows, Ann. Rev. Fluid Mech. 30 (1998) 329–364.
[4] A.J. Chorin, The numerical solution of the Navier–Stokes equations for an incompressible fluid, Bull. Am. Math. Soc. 73 (1967) 928–931.
[5] A.J. Chorin, A numerical method for solving incompressible viscous flow problems, J. Comput. Phys. 2 (1967) 12–36.
[6] A.J. Chorin, Numerical solution of the Navier–Stokes equations, Math. Comput. 22 (1968) 745–762.
[7] W. E, J.-G. Liu, Vorticity boundary condition and related issues for finite difference schemes, J. Comput. Phys. 124 (1996) 368–382.
[8] W. E, J.-G. Liu, Essentially compact schemes for unsteady viscous incompressible flows, J. Comput. Phys. 126 (1996) 122–138.
[9] W. E, J.-G. Liu, Gauge method for viscous incompressible flows, J. Comput. Phys., to appear.
[10] U. Ghia, K.N. Ghia, C.T. Shin, High-*Re* solutions for incompressible flow using the Navier–Stokes equations and a multigrid method, J. Comput. Phys. 48 (1982) 387–411.
[11] D. Givoli, J.E. Flaherty, M.S. Shephard, Parallel adaptive finite element analysis of viscous flows based on a combined compressible–incompressible formulation, Int. J. Numer. Methods Heat Fluid Flow 7 (1997) 880–906.
[12] J.L. Guermond, L. Quartapelle, Calculation of incompressible viscous flows by an unconditionally stable projection FEM, J. Comput. Phys. 132 (1997) 12–33.
[13] B. Gustafsson, H. Stoor, Navier–Stokes equations for almost incompressible flow, SIAM J. Numer. Anal. 28 (1991) 1523–1547.
[14] H. Han, W. Bao, An artificial boundary condition for the incompressible viscous flows in a no-slip channel, J. Comput. Math. 13 (1995) 51–63.
[15] G. Hauke, T.J.R. Hughes, A unified approach to compressible and incompressible flows, Comput. Methods Appl. Mech. Engrg. 113 (1994) 389–395.
[16] S. Hou, Q. Zou, S. Chen, G. Doolen, A.C. Cogley, Simulation of cavity flow by the lattice Boltzmann method, J. Comput. Phys. 118 (1995) 329–347.
[17] S. Klainerman, A. Majda, Singular limits of quasilinear systems with large parameter and the incompressible limit of compressible fluids, Comm. Pure Appl. Math. 34 (1981) 481–524.
[18] S. Klainerman, A. Majda, Compressible and incompressible fluids, Comm. Pure Appl. Math. 35 (1982) 629–651.

[19] R. Klein, Semi-implicit extension of a Godunov-type scheme based on low Mach number asymptotic I: one-dimensional flow, J. Comput. Phys. 121 (1995) 213–237.
[20] R. Klein, C.D. Munz, The extension of incompressible flow solvers to the weakly compressible regime, preprint.
[21] L.D. Landau, E.M. Lifshitz, Fluid Mechanics, Pergamon Press, Oxford, 1987.
[22] C.K. Lin, On the incompressible limit of the compressible Navier–Stokes equations, Comm. Partial Differential Equations 20 (1995) 677–707.
[23] A. Majda, Compressible Fluid Flow and System of Conservation Laws in Several Space Variables, Appl. Math. Sci. 53, Springer, Berlin, 1984.
[24] C.J. Ribbens, L.T. Watson, C.Y. Wang, Steady viscous flow in a triangular cavity, J. Comput. Phys. 112 (1994) 173–181.
[25] J. Shen, On a new pseudo-compresibility method for the incompressible Navier–Stokes equations, Appl. Numer. Math. 21 (1996) 71–90.
[26] R. Temam, Sur l'approximation de las solution des equations de Navier–Stokes par la méthode des fractionnairires II, Arch. Rational Mech. Anal. 33 (1969) 377–385.
[27] T.E. Tezduyar, J. Liou, D.K. Ganjoo, M. Behr, Solution techniques for the vorticity-streamfunction formulation of two-dimensional unsteady incompressible flows, Int. J. Numer. Methods Fluids 11 (1990) 515–539.
[28] S. Ukai, The incomrpessible limit and the initial layer of the compressible Euler equations, J. Math. Kyoto Univ. 26 (1986) 323–331.
[29] R. Vichnevtsky, Stability charts in the numerical approximation of partial differential equations: a review, Math. Comput. Simulation XXI (1979) 170–177.
[30] R. Vichnevetsky, Stability charts of methods of lines for partial differential equations, in: Proceedings of the Sixth Annual Princeton Conference on Information Science and Systems, Princeton University, 1972, pp. 307–312.